JOURNAL OF AIRCRAFT
Vol. 45, No. 4, July–August 2008

Lift from Spanwise Flow in Simple Flapping Wings

YoungSun Hong* and Aaron Altman†
University of Dayton, Dayton, Ohio 45469-0238

DOI: 10.2514/1.34100

Spanwise flow contributes to lift in thin flat-plate zero-pitch-angle flapping wings in quiescent air. It is reasonable to maintain only the kinematics and mechanical complexity absolutely necessary in developing flapping-wing micro air vehicles. This study continues the quantification of the lift generated from a flapping motion of absolute minimum complexity thought to be capable of generating lift. A flapping-wing micro air vehicle with rectangular planform wings fabricated in-house (semispan aspect ratios from 1.5 to 4.0) was used to quantify the contributions to lift from flow along the span of wings at numerous points throughout the flapping cycle under a variety of operating conditions (3–6 Hz and Reynolds numbers of 6000–15,000). These experiments were performed for several aspect ratios for flat-plate and spanwise-cambered wings. The lift force was quantified experimentally using a force transducer and a high-speed camera. Digital particle image velocimetry was used to determine the lift contributions of spanwise flow to the total measured lift. Additionally, the presence of spanwise camber was shown to affect the transient lift behavior.

Nomenclature

A	=	axial force
a_T	=	tangential acceleration
D	=	drag
L	=	lift
N	=	normal force
P_u, P_l	=	pressure over the upper and lower surfaces of the wing
R	=	resultant force
S^*	=	normalized speed (instantaneous speed divided by the average speed of the wing frame of reference for one cycle)
T^*	=	normalized time (temporal location in the flapping cycle multiplied by the flapping frequency), instantaneous time divided by the total time for one period
V^*	=	normalized velocity (local flow velocity divided by the instantaneous wingtip speed)
$\mathbf{V}_{\text{rf}}$	=	velocity of the control-volume reference frame
V_T	=	tangential velocity
$\mathbf{V}_{XYZ}$, $\mathbf{V}_{\text{xyz}}$	=	velocity with respect to the inertial frame (XYZ) and reference frame (xyz)
α	=	angular acceleration
θ	=	angle of the flapping wing along the flap arc
τ_u, τ_l	=	shear stress over the upper and lower surfaces of the wing
Φ	=	wing-beat amplitude (peak to peak), rad
ω	=	angular velocity

Introduction

THE operational limitations of fixed-wing micro air vehicles (MAVs) have been suitably investigated such that these limitations and opportunities for growth are well understood. The most limiting areas are generally accepted to be gust tolerance and maneuverability. These limitations have spurred interest in flapping- and rotary-wing MAV development. A number of commercial ornithopters are available for purchase, and several others have been developed at academic institutions. In general, these ornithopters offer limited range and limited payload and are incapable of hover. The process used to arrive at the commercially available ornithopter designs is proprietary and the development is often based on a trial-and-error approach to optimization.

Much work has been published in an effort to better understand both bird and insect flight. Most efforts focus on deconstructing animal kinematic motion into its constitutive elements and deducing or measuring the aerodynamic effects of these motions. At a workshop sponsored by the U.S. Air Force Office of Scientific Research on biologically inspired flight for MAVs [1] in June 2006, a consensus was reached among numerous experts in flapping-wing fluid physics that the study of animal flight and creating commercial ornithopters left some fundamental questions unanswered. It was the recommendation of the workshop fluid physics group from the perspective of flapping-wing MAV development that a set of canonical problems be developed from the simplest possible cases, with complexity added to subsequent iterations. It was believed that these canonical problems could provide some context for the much more complex and unsteady aerodynamics associated with real animal flapping kinematics. One of the simple cases proposed for study was pure flapping in quiescent air, which is the topic of the present study.

Several mechanisms unique to the flapping motion in flapping wings can produce strong spanwise flow. This spanwise flow is often associated with the leading-edge vortex as axial flow in the core of the vortex [2,3]. This flow characteristic has been largely ignored, with the exception of its suspected contribution to the stabilization of the leading-edge vortex. Spanwise flow can be defined as flow that travels along the span of the wing from the root to the tip, more or less parallel to the leading edge. It can also be defined as any flow in the spanwise plane. In fixed wings, spanwise flow is generally regarded as a disadvantage, due to the related induced drag. However, when applied to flapping-wing aerodynamics, spanwise flow has been identified as a potentially key characteristic to the generation of lift [2,3].

Spanwise Flow and the Wingtip Vortex Effect

Fixed Wing

There is a miniscule component of flow in the spanwise direction over the finite wing in steady level flight at the root that gradually increases toward the tip. A spanwise component of flow from the tip toward the wing root causes the streamlines over the top surface to bend toward the root and causes those over the bottom surface to

Presented as Paper 0448 at the 44th AIAA Aerospace Sciences Meeting and Exhibit, Reno, NV, 9–12 January 2006; received 17 August 2007; revision received 8 February 2008; accepted for publication 14 February 2008. Copyright © 2008 by the American Institute of Aeronautics and Astronautics, Inc. All rights reserved. Copies of this paper may be made for personal or internal use, on condition that the copier pay the $10.00 per-copy fee to the Copyright Clearance Center, Inc., 222 Rosewood Drive, Danvers, MA 01923; include the code 0021-8669/08 $10.00 in correspondence with the CCC.

*Graduate Student, Department of Mechanical and Aerospace Engineering, 300 College Park; currently, Major, Korean Air Force. Student Member AIAA.

†Assistant Professor, Department of Mechanical and Aerospace Engineering, 300 College Park. Associate Fellow AIAA.

bend toward the tip. This is shown in an exaggerated form in Fig. 1. In Fig. 1a, higher-pressure air on the wing's lower surface flows around the wingtip to the upper surface, influencing spanwise flow at the tip. Figure 1b shows the spanwise-flow effects on chordwise flow on a finite wing; solid lines represent the upper surface and dashed lines represent the lower surface.

More pronounced spanwise-flow effects can be seen in wings with sweep. However, spanwise flow is generally regarded as one of the disadvantages of swept wings, due to the related induced drag. There is an increase in the lift near the tip of a swept-back wing and a decrease in lift near the root. One of the extreme examples of these swept-wing effects can be seen with the delta wing. Delta wings are tremendously effective in lift at low speeds and unsteady flows (Taylor et al. [4]). Their leading-edge vortices induce a field of low pressure on the suction side of the wing. However, research on swept-back and delta wings has, for the most part, focused on the disadvantages of spanwise flow and the vortex effects on lift. Despite the wealth of research performed relating lift to wingtip vortex circulation and behavior in traditional fixed wings, there has been little published that attempts to quantify the direct contribution of only spanwise flow to the lift force in flapping wings.

Flapping Wings

As previously stated, spanwise flow has been identified in the form of axial flow within the leading-edge vortex in flapping wings [2,3], and the magnitude of flow in the spanwise direction can be greater than in the chordwise direction, depending on the forward velocity and rotational motion [5]. Figure 2 demonstrates that the span of the wings of over 1000 birds and insects taken from the data of Greenewalt [6] correlate well with the flapping frequency for birds and correlates reasonably well with body mass. These relationships could potentially be purely coincidental; however, they could also be indicative of the relative importance of the spanwise direction in the aerodynamics of birds and insects. No similar correlations exist for the chordwise direction or wing areas of birds and insects, as can be seen in the data of Azuma [7].

Experimental Approach

In an effort to reduce the problem to its simplest form and to isolate the effects of spanwise flow, flat-plate wings (and, later, spanwise-cambered plates) were given a single-hinged pure flapping motion (downstroke and upstroke) with no flapping-stroke-plane inclination angle. The chordwise pitch angle was fixed at 0 deg (perfectly horizontal, as viewed from the tip). The experiments were performed in quiescent air in a cube-shaped enclosure greater than 1 m in each dimension. In addition, this experimental setup guarantees that the origin of any spanwise flow is independent of freestream influence and is due explicitly to the pure flapping motion itself. The effects of wake capture were not isolated because the study was intended merely to identify the contributions of spanwise flow and not to isolate every possible contributor to the origins or interactions of this spanwise flow.

To determine the total aerodynamic force contribution of spanwise flow, this contribution was first isolated and quantified. The total force generated was measured with a force transducer. Inertial and added mass effects were then considered, and this procedure will be explained further in the next section. In this experiment, a high-frame-rate camera was used to take images of the flapping mechanism/wing using a fixed frame rate (constant time interval between images).

With an isolated aerodynamic force, digital particle image velocimetry (DPIV) was used to determine velocity distributions over the wing. Contributions to lift force due to vorticity and circulation were addressed in a separate paper [8]. The force distribution along the span and the force variation during the flapping cycle were estimated using several different methods: 1) a control-volume approach and 2) a pressure and shear force distribution based on the velocity data obtained from the results of DPIV. These methods will be described in detail in a subsequent section.

Experimental Setup

The total lift force was measured using an S-beam force transducer (Interface SSM-AJ-250) with a maximum error of 0.025 lb, a maximum nonrepeatability of less than 0.02%, and a maximum creep in 20 min of less than 0.025%. The net aerodynamic force was determined from this measured total force by subtracting the

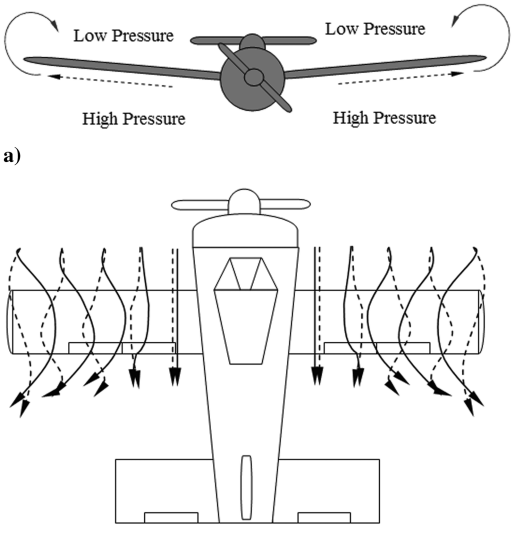

Fig. 1 Spanwise flow: a) front view and b) top view.

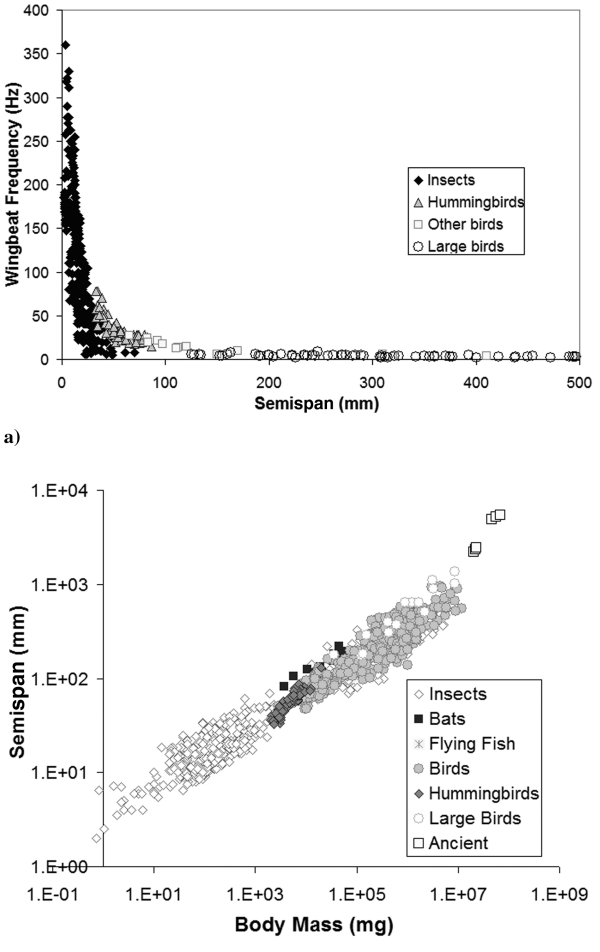

Fig. 2 Correlations between [11] a) wing-beat frequency vs wing semispan of various insects and birds and b) wing semispan vs body mass of various animals including insects, bats, and birds.

experimentally determined inertial contribution. A high-frame-rate camera (Fastcam Ultima ADX, 1000 frames/second) was used to permit experimental determination of the inertial forces of the flapping mechanism.

The inertial force was defined as the force due to mass and acceleration of the flapping mechanism, and it can be obtained using Newton's second law ($F = ma$). Angular velocity and angular acceleration were obtained by analyzing these images. The forces in the x and y directions of the flapping mechanism were calculated using angular velocity and angular acceleration and assuming uniform mass distribution:

$$\omega = \frac{\Delta\theta}{\Delta t} \tag{1a}$$

$$\alpha = \frac{\Delta\omega}{\Delta t} \tag{1b}$$

$$V_T = r\omega \tag{1c}$$

$$a_T = r\alpha \tag{1d}$$

Flapping angles were then used to generate the inertial force distribution from a set of experimentally determined discrete points. To obtain the inertial force variation, the smoothed flapping-angle distribution was approximated with a fourth-order (or greater) polynomial curve fit. Then, using $F = ma$ and Eq. (1), the inertial force in the y axis (the axis aligned with lift and gravity) was obtained.

For Sane and Dickinson's [9] experimental setup, added mass inertia effects for an infinitesimally thin two-dimensional plate in an inviscid fluid were relatively small. Although they were using kinematics that were dissimilar to those used in this study, there were regions in which the motion was similar. In the regions in which linear velocity of the wing was not constant, the contributions of added mass inertia were still quite small. In addition, their study was performed in mineral oil with a density several orders of magnitude greater than air. Because this paper is focused specifically on determining the relative magnitude of the spanwise-flow contribution to the overall lift force, rather than an exact accounting of all measured force, it is reasonable to consider the effects of added mass inertia to be some small component contained within the resulting aerodynamic force component.

Figure 3 shows the DPIV setup for the experiment. A Megaplus ES 1.0 camera was used, operating in the frame-straddling mode of image acquisition required for the short interframe times required for PIV image acquisition. The camera synchronization with the frame grabber (EPIX) and laser firing (Spectra Physics, double-pulsed 300 mJ/pulse, 10 pulse/s Nd:YAG) was controlled via the strobe signal of the camera. The delay generator (Stanford Research DG 535) was used to trigger the PIV laser flash lamps and Q switches. The pulse that sends a signal started all of the timing events and was in phase with the laser repetition rate. The trigger pulse from the flapping motion was used to trigger the camera. To trigger the pulse using the flapping motion, an emitter and detector were installed and aligned with the peak of the flapping motion. When the flapping wings interrupted the beam, the detector produced a regular signal. The laser beam used for PIV was split through a cylindrical lens to generate the light sheet. The light scattered by the smoke particles (0.2–2 μm) was recorded on a 1×1 k 8-bit progressive-scan CCD camera using a 25-mm Cosmicar C-mount lens at a lens aperture setting of 6. The PIV images were taken at numerous locations along the span and at numerous chordwise stations (Fig. 4). In Fig. 4a, points 1 and 3 denote the camera field of view (FOV) with the laser sheet oriented in the spanwise plane (leading edge and trailing edge), and points 2 and 4 denote the FOV with the laser sheet oriented in the chordwise plane (wingtip and the middle of the wing). The solid lines denote the plane of the laser sheet, and the dashed lines denote the spanwise plane and chordwise plane. In Fig. 4b, points 1–4 denote the FOV with the laser sheet oriented in the spanwise plane (from wingtip to wing root at the leading edge). In both Figs. 4a and 4b, the dotted vertical lines indicate the intersections between planes in which the velocities perpendicular to the wing surface in both images should be the same. The composite image plane was taken at a distance of 5 mm from the wing edge.

DPIV V2.0 (Innovative Scientific Solutions, Inc.) was used for postprocessing using a 64-pixel correlation size and a 50% image overlap. The field of view was 4.3×4.3 cm, pulse separation time was 50 μs, and a minimum average of 20 particles per interrogation region was used. Employing the induced particle velocity method of Westerweel [10] and taking into consideration the maximum acceleration seen in the experiment, an error in velocity of less than 0.5% can be expected.

Flapping Mechanism and Wings

The flapping mechanism was adapted from a Cybird P1 remote control ornithopter model (Fig. 5a). In this experiment, the flapping mechanism was powered by an external dc power supply. Depending upon the wing type, the operating angle was a weak function of flapping frequency. This was believed to result from lash in the mechanism, but was not believed to have been significant enough to affect the predicted aerodynamic force once the inertial effects were removed. Wing deflection was determined to be nominal through the use of the high-speed camera. The frequency of 4 Hz was selected

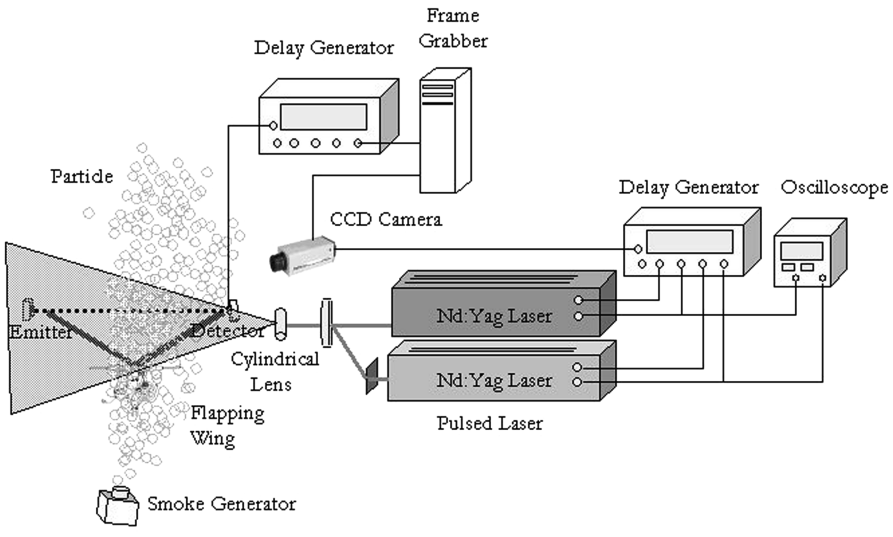

Fig. 3 Experimental setup with DPIV.

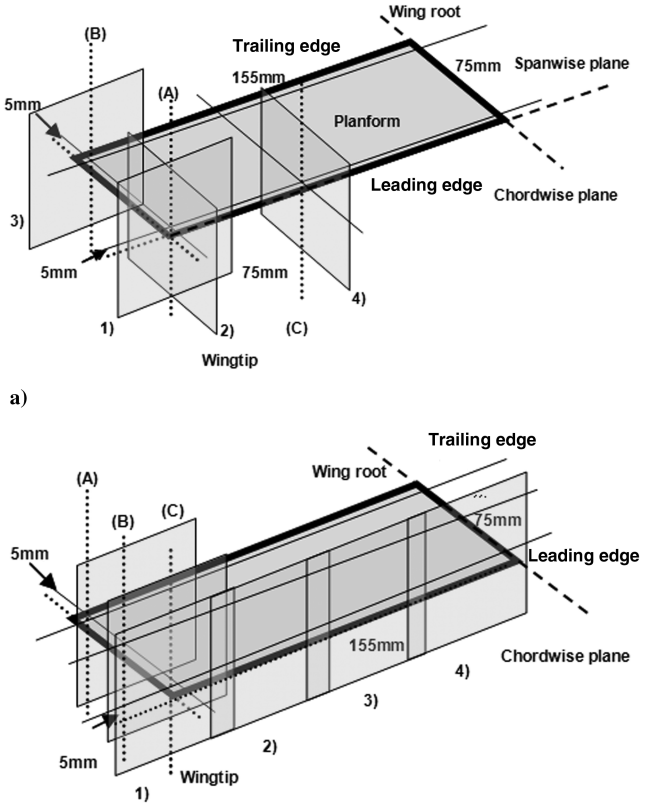

Fig. 4 PIV image planes: a) spanwise plane at the leading-edge point 1 and trailing-edge point 3 and chordwise plane at the wingtip point 2 and middle of the wing point 4 and b) PIV image plane composite used to image the entire wing.

from the data of Alford and Altman [11], which demonstrated a strong correlation between span and flap frequency for animals flapping in air. The flapping frequency was set using a high-precision strobe and remained constant to within roughly 1.5%. Table 1 shows the properties of the various wings used in the experiment. The wing thickness was 0.3 mm. The wing frame was composed of a carbon fiber rod, and the wing-covering material was rigid and optically transparent.

Figure 5b provides the various rectangular wing planforms used in the experiments. Only wing type B was used to generate the data presented in this paper. Figure 5c provides a reference coordinate system. The operating angle of the flapping mechanism with the uncambered wing was $\alpha = 41$ deg, $\beta = 18$ deg, $t' = 0.116$, and $t'' = 0.250$ at a flapping frequency of 4 Hz with wing no. 4. The cambered and flat-plate wings have the same mass, material, area, and aspect ratio (wing nos. 4 and 6 in Table 1). The cambered wing was only cambered in the spanwise direction, as seen in Fig. 5d. The spanwise-cambered shape in wing no. 6 can be duplicated as follows:

$$\frac{y}{b} = -0.002\left(\frac{x}{b}\right)^3 + 0.0176\left(\frac{x}{b}\right)^2 - 0.0371\left(\frac{x}{b}\right) + 2.7819$$

The operating angle of the flapping mechanism with the wing cambered in span was $\alpha = 40$ deg, $\beta = 19$ deg, $t' = 0.114$, and $t'' = 0.248$ at a flapping frequency of 4 Hz with wing no. 6. The shaded squares covering the region around the tips of the wings in Figs. 5c and 5d represent sample PIV image planes.

Force Variation During the Flapping Cycle: Time History of Flapping Motion

The following results relating to the time history of the flapping motion are restated here for clarity and continuity from the data of Hong and Altman [8]. An example of flapping-angle variation with time can be seen in Fig. 6a for the 4-Hz case (0.25-s period) with wing no. 2 from Table 1. In this figure, it is evident that there is a slight

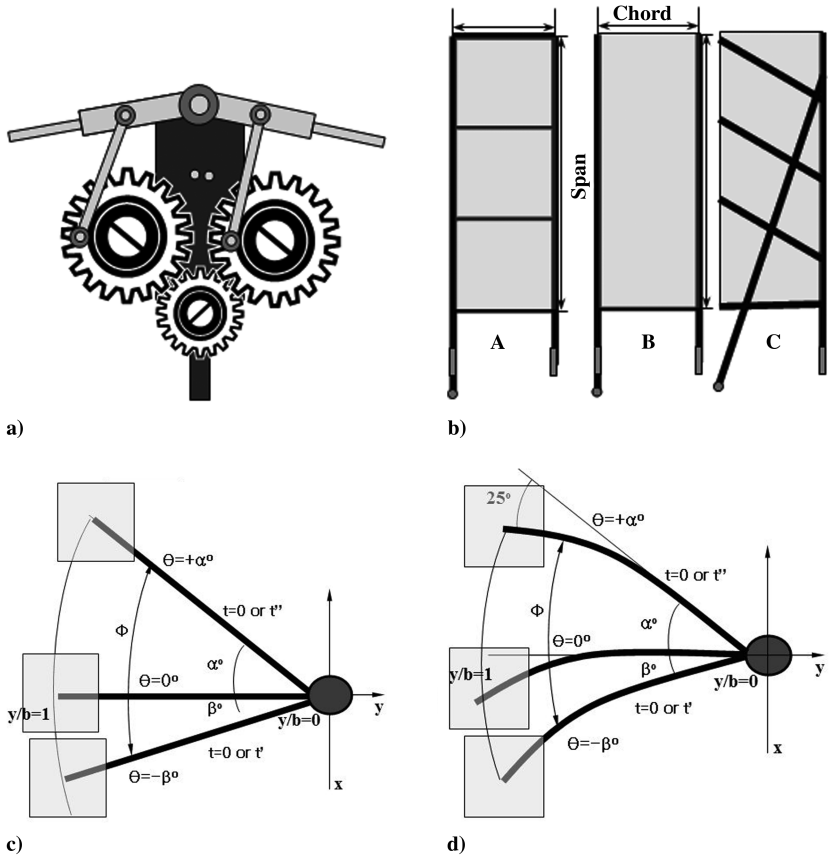

Fig. 5 Details of the flapping mechanism, wings, and coordinate systems used: a) flapping mechanism, b) various wing planforms tested, c) coordinate system definition for the uncambered (span) wing, and d) coordinate system for the wing cambered in span.

asymmetry in the flapping motion. The time spent in the downstroke is 0.116 s ($0 < T^* < 0.464$), leaving 0.134 s ($0.464 < T^* < 1$) in the upstroke. This yields average speeds of 1.91 and 1.52 m/s in the downstroke and upstroke, respectively, with maximum speeds of 3.7 and 2.8 m/s in the downstroke and upstroke, respectively. The effects of this asymmetry will be seen later in differences in the up- and downstroke velocity and force distributions. Also in Fig. 6a, the approximated curve fit can be seen superimposed over the experimental results. For the same (experimental) case, the tangential velocity calculated at the tip of the wing using the variation in flapping angle with time can be seen in Fig. 6b, along with a polynomial-curve-fit approximation. It was necessary to create a smoothed approximation curve to the tangential velocity, because it was subsequently used to derive the acceleration. Figure 6b more clearly shows the typical relative time spent in the up- and downstrokes. The magnitude of the maximum velocity in the downstroke is clearly greater than in the upstroke. The tangential acceleration variation with time can be seen in Fig. 6c. As expected, the maximum accelerations occur in the transitions from downstroke to upstroke and vice versa. It is noted that the tangential acceleration was multiplied by -1 to translate the force-transducer sign convention to the same convention used later in the analysis.

Force from Inertia

Inertial forces shown herein represent the acceleration force on the mass of the wing. The aforementioned representative results from the high-frame-rate camera were used to generate the inertial force distribution, which is presented both in (corrected) raw form and in the form of an approximated polynomial curve fit. Figure 7a shows the total lift variation and the inertial variation throughout the entire cycle, from the beginning of the downstroke to the end of upstroke, for a typical data set. As is commonly seen in the literature for experiments conducted in air, the inertial force is roughly of the same order of magnitude as the aerodynamic force. These trends were observed at flapping frequencies of 3, 4, 5, and 6 Hz.

Figure 7b shows the resulting lift contribution to the aerodynamic force, in which the inertial force is subtracted from the total measured lift force. At the beginning of the downstroke and at the end of the upstroke, the inertial force is greater than the total measured force. This is due to a negative aerodynamic lift force (Fig. 7b), which cancels out the inertial contribution. It is noted that the trends for temporal variation in total aerodynamic lift force and measured total lift force are similar in shape throughout most of the flapping cycle.

Analysis of the Forces Resulting from Flow in the Spanwise Direction

To evaluate the force variation of an entire cycle of flapping motion using PIV results, two common methods are used to determine the instantaneous force: the direct evaluation of the combination of the pressure and the shear stress on the surface of the wing [12] and a momentum-based method using a moving control volume [13,14]. The aerodynamic forces and moments on the wing come from two basic sources: pressure/velocity distribution over the wing surface and shear stress distribution over the body surface. Although the momentum-based method has been shown to be less accurate [15], it has also been shown to be accurate well within an order of magnitude, which is sufficient to demonstrate the importance of the contributions of spanwise flow to the generation of lift in this particular experimental implementation.

Table 1 Characteristics of the wings used in the experiment

Wing no.	Semispan, cm	Chord, cm	Aspect ratio	Type	Mass, g
1	20.00	10.00	4.00	A	15.99
2	15.00	10.00	3.00	C	9.79
3	15.00	7.50	4.00	C	7.78
4	15.50	7.50	4.10	B	7.34
5	5.50	7.50	1.50	B	3.48
6	15.50	7.50	4.10	B	7.34

As seen in Fig. 8, normal force N is the component of the resultant force R perpendicular to the wing. Axial force A is the component of the resultant force R parallel to the wing. The normal and axial forces acting on the wing surface are

$$N = -\int P_u \, dS_u + \int P_l \, dS_l \tag{2}$$

$$A = \int \tau_u \, dS_u + \int \tau_l \, dS_l \tag{3}$$

Lift L is defined as the component of the resultant force R and the component of force opposite to gravity, and drag D is defined as the component of the force perpendicular to the lift force L. The pressure

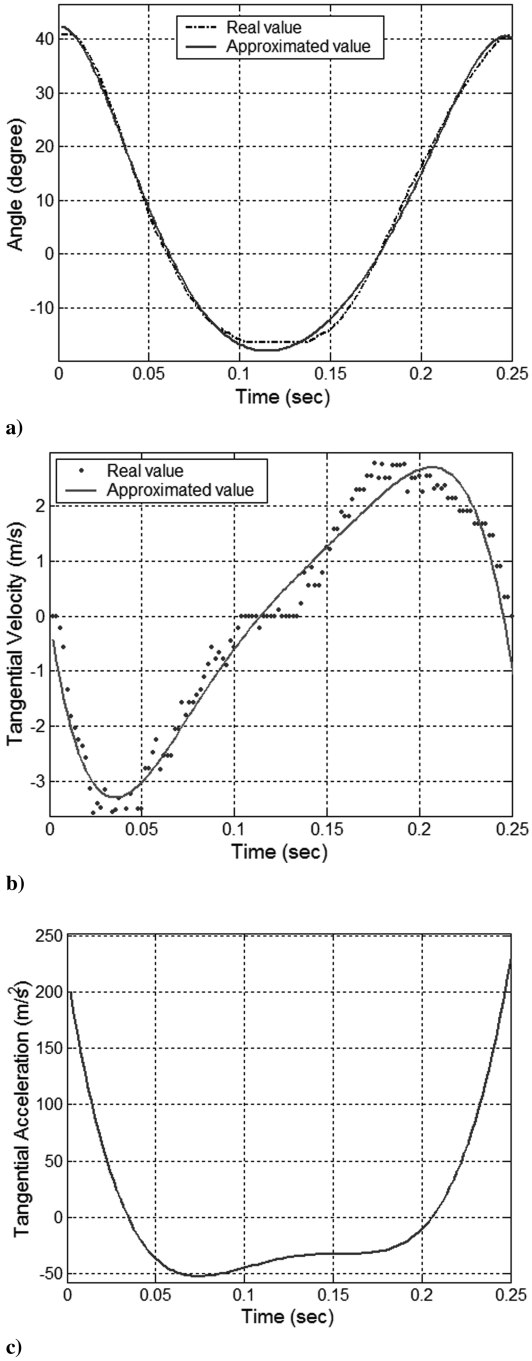

Fig. 6 One complete cycle of flapping angle, tangential velocity and acceleration variation using real data and approximate curve fits for wing no. 2 flapping at 4 Hz. (The bottom figure was multiplied by −1 to maintain the same sign convention as used with the force transducer.)

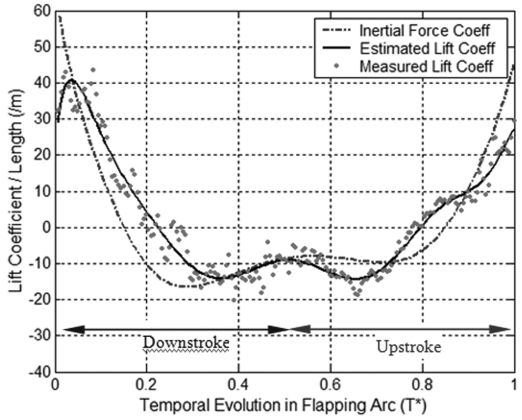

a)

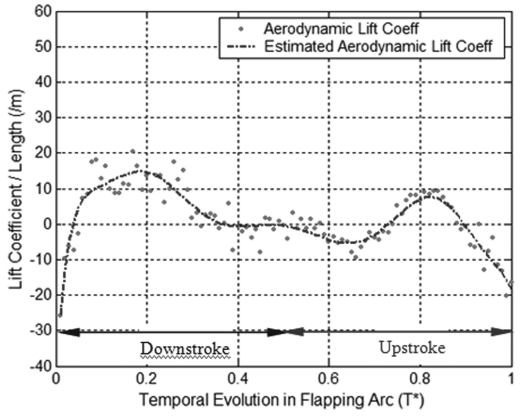

b)

Fig. 7 Temporal variation in force coefficient using wing no. 2 at a 5-Hz flapping frequency during one complete cycle: a) total force coefficient, including the inertia force coefficient and b) isolated aerodynamic force coefficient.

and the shear stress method are formulated as follows:

$$L = \int [-P_u \cos\theta - \tau_u \sin\theta]\,\mathrm{d}S_u + \int [P_l \cos\theta - \tau_l \sin\theta]\,\mathrm{d}S_l \quad (4)$$

$$D = \int [-P_u \sin\theta + \tau_u \cos\theta]\,\mathrm{d}S_u + \int [P_l \sin\theta + \tau_l \cos\theta]\,\mathrm{d}S_l \quad (5)$$

The pressure distribution along the wing surface can also obtained by integrating the momentum equations (6) and (7) [14] along the x and y directions or from the pressure Poisson equation (8) [16] while making fewer assumptions:

$$\frac{\partial u}{\partial t} + u\frac{\partial u}{\partial x} + v\frac{\partial u}{\partial y} = -\frac{1}{\rho}\frac{\partial p}{\partial x} + \frac{\mu}{\rho}\left[\frac{\partial^2 u}{\partial x^2} + \frac{\partial^2 u}{\partial y^2}\right] \quad (6)$$

$$\frac{\partial v}{\partial t} + u\frac{\partial v}{\partial x} + v\frac{\partial v}{\partial y} = -\frac{1}{\rho}\frac{\partial p}{\partial y} + \frac{\mu}{\rho}\left[\frac{\partial^2 v}{\partial x^2} + \frac{\partial^2 v}{\partial y^2}\right] \quad (7)$$

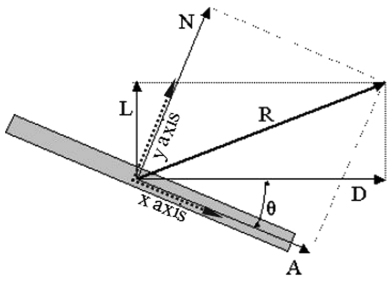

Fig. 8 Applied force along the wing.

$$\nabla^2 p = -\rho\nabla\cdot(u\cdot\nabla u) = -\rho\left[\left(\frac{\partial u}{\partial x}\right)^2 + \left(\frac{\partial v}{\partial y}\right)^2 + 2\frac{\partial u}{\partial y}\frac{\partial v}{\partial x}\right] \quad (8)$$

where u and v are velocities in the x and y directions. The x and y axes are defined as the parallel and perpendicular axes of the flat-wing surface (Fig. 8). Initially, several simplifying assumptions will be made. Increasing complexity will be introduced into the solution later in this section. For the most simplified approach used here, the following assumptions are made:

The flow is steady ($\partial u/\partial t = 0$ and $\partial v/\partial t = 0$, taken as a snapshot in time), incompressible (ρ is a constant), irrotational ($\nabla \times V = 0$) flow along a streamline. With these assumptions for the simplified case, the incompressible Bernoulli equation can be used to obtain the pressure distribution along the wing:

$$p = p_\infty - \tfrac{1}{2}\rho V^2 \quad (9)$$

Application of a momentum-based method using a moving control volume can also determine the force generated by the flapping wing using PIV velocity data. The velocities of the control volumes in the x and y directions (U_i and V_i) are determined from the results of analysis of images taken with a high-frame-rate camera (Fastcam Ultima ADX, 1000 frames/second). PIV results provide the velocity data along the wing during the flapping motion (Fig. 9). If the flapping wing and the area immediately surrounding it are defined as the control volume, the wing can be divided into several smaller control volumes. Each smaller control volume includes a velocity vector over the wing and under the wing (Fig. 10). As a result, the momentum equation for accelerating control volumes is applied to the total control volume, which includes wing and velocity vectors along the wing. Because there is some ambiguity in the literature regarding the definitions used for the Reynolds number in flapping wings, the definition used is presented here for clarity. A mean Reynolds number for hovering flight based on the mean chord ($c = 2l/AR$) and the mean wingtip velocity ($U = 2\Phi f l$) is defined as follows [17]:

$$Re = \frac{\rho c U}{\mu} = \frac{\rho \Phi f l^2}{\mu AR} \quad (10)$$

For an inertial control volume, the appropriate formulation of Newton's second law is given by

$$\mathbf{F} = \frac{\partial}{\partial t}\int_{\mathrm{cv}} \mathbf{V}_{XYZ}\rho_{\mathrm{cv}}\,\mathrm{d}\forall + \int_{\mathrm{CS}} \mathbf{V}_{XYZ}\rho_{\mathrm{cs}}\mathbf{V}_{\mathrm{xyz}}\cdot\,\mathrm{d}\mathbf{A} \quad (11)$$

The velocity with respect to the inertial frame (XYZ) and the reference frame (xyz) is related by the relative motion equation:

$$\mathbf{V}_{\mathrm{xyz}} = \mathbf{V}_{\mathrm{XYZ}} - \mathbf{V}_{\mathrm{rf}} \quad (12)$$

From Eq. (11),

$$\mathbf{F} = \mathbf{F}_{\mathrm{surface}} + \mathbf{F}_{\mathrm{body}} + \mathbf{F}_{\mathrm{resultant}} \quad (13)$$

where surface force $\mathbf{F}_{\mathrm{surface}}$ is the sum of the pressure and shear force:

$$\mathbf{F}_{\mathrm{surface}} = \mathbf{F}_{\mathrm{pressure}} + \mathbf{F}_{\mathrm{shear}}$$

$\mathbf{F}_{\mathrm{body}}$ is the body force and $\mathbf{F}_{\mathrm{resultant}}$ is the resultant force, which exerts equal and opposite pressure and shear force distribution on the flow over the body by Newton's third law. Therefore, Eq. (11) becomes

$$\mathbf{F}_{\mathrm{pressure}} + \mathbf{F}_{\mathrm{shear}} + \mathbf{F}_{\mathrm{body}} + \mathbf{F}_{\mathrm{resultant}} = \frac{\partial}{\partial t}\int_{\mathrm{cv}} \mathbf{V}_{\mathrm{XYZ}}\rho_{\mathrm{cv}}\,\mathrm{d}\forall + \int_{\mathrm{CS}} \mathbf{V}_{\mathrm{XYZ}}\rho_{\mathrm{cs}}\mathbf{V}_{xyz}\cdot\,\mathrm{d}\mathbf{A} \quad (14)$$

If flow is inviscid and $\mathbf{F}_{\mathrm{body}} \ll \mathbf{F}_{\mathrm{pressure}}$ because the control volume is selected around the air, then the shear forces $\mathbf{F}_{\mathrm{shear}}$ and body forces $\mathbf{F}_{\mathrm{body}}$ have nominal values and can be omitted. Therefore, Eq. (13) becomes

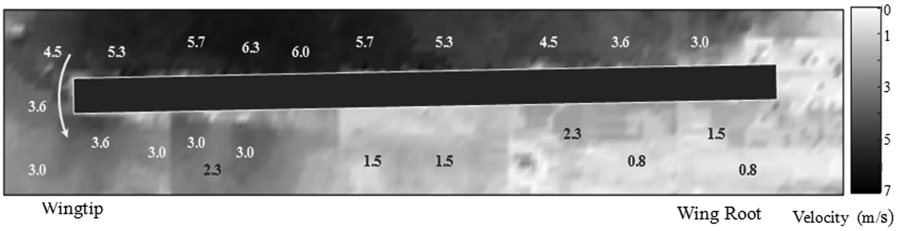

Fig. 9 Contour plot of the magnitude of the velocity field composed of instantaneous PIV images taken along the entire semispan of the wing at the same location in the downstroke ($\Phi = -2$ deg) at a 4-Hz flapping frequency ($Re = 14,700$) with wing no. 1.

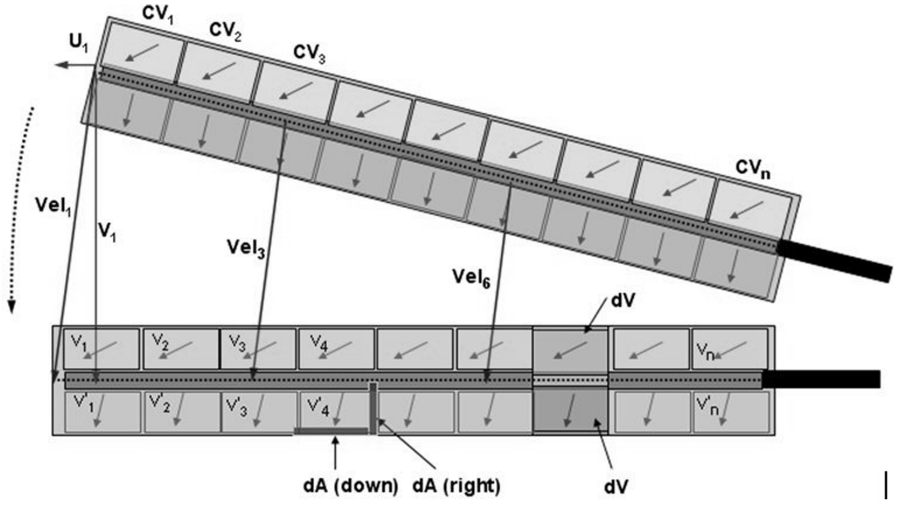

Fig. 10 Control volume to calculate the instantaneous force around the flapping wing.

$$\mathbf{F}_{\text{resultant}} \approx -\mathbf{F}_{\text{pressure}} + \frac{\partial}{\partial t}\int_{\text{cv}} \mathbf{V}_{\text{XYZ}}\rho_{\text{cv}}\,\text{d}\cancel{V} + \int_{\text{CS}} \mathbf{V}_{\text{XYZ}}\rho_{\text{cs}}\mathbf{V}_{xyz}\cdot\,\text{d}\mathbf{A} \tag{15}$$

The resultant force (lift or drag) is equal to the sum of the pressure force (or normal force N), the time rate of change of the momentum inside the control-volume selection, and the net rate of momentum flux out through the control surface.

The sum of the time rate of change of the momentum inside the control-volume selection and the net rate of momentum flux out through the control surface in the y direction can then be written as follows:

$$\begin{aligned}
&\frac{\partial}{\partial t}\int_{\text{cv}} \mathbf{V}_{\text{XYZ}}\rho_{\text{cv}}\,\text{d}\cancel{V} + \int_{\text{cs}} \mathbf{V}_{\text{XYZ}}\rho_{\text{cs}}\mathbf{V}_{xyz}\cdot\,\text{d}\mathbf{A}\\
&= \sum_{i=1}^{n}\Bigg[\frac{\text{d}}{\text{d}t}\int_{\text{cv(upper)}} \rho_{v_{yi}}\,\text{d}\cancel{V} + \int_{\text{cs(upper}_{\text{LH}})} v_{yi}\rho[(v_{xi}-U_i)\cos\alpha\\
&-(v_{yi}-V)\sin\alpha]\cdot n\,\text{d}\mathbf{A} + \int_{\text{cs(upper}_{\text{RH}})} v_{yi}\rho[(v_{x(i+1)}-U_i)\cos\alpha\\
&-(v_{y(i+1)}-V_i)\sin\alpha]\cdot n\,\text{d}\mathbf{A} + \int_{\text{cs(upper}_{\text{top}})} v_{yi}\rho[(v_{xi}-U_i)\sin\alpha\\
&-(v_{yi}-V_i)\cos\alpha]\cdot n\,\text{d}\mathbf{A} + \frac{\text{d}}{\text{d}t}\int_{\text{cv(lower)}} \rho v'_{yi}\,\text{d}\cancel{V}\\
&+\int_{\text{cs(lower}_{\text{LH}})} v'_{yi}\rho[(v'_{xi}-U_i)\cos\alpha-(v'_{yi}-V_i)\sin\alpha]\cdot n\,\text{d}\mathbf{A}\\
&+\int_{\text{cs(lower}_{\text{RH}})} v'_{yi}\rho[(v'_{x(i+1)}-U_i)\cos\alpha-(v'_{y(i+1)}-V_i)\sin\alpha]\cdot n\,\text{d}\mathbf{A}\\
&+\int_{\text{cs(lower}_{\text{bottom}})} v'_{yi}\rho[(v'_{xi}-U_i)\sin\alpha-(v'_{yi}-V_i)\cos\alpha]\cdot n\,\text{d}\mathbf{A}\Bigg]
\end{aligned} \tag{16}$$

where V_i and U_i are the y and x components of the control-volume velocity, respectively; v_{xi} and v'_{xi} (v_{yi} and v'_{yi}) are the x components (y components) of the air flow velocity (v_i and v'_i in Fig. 10) over the upper and lower surfaces of the wing; α is the angle of the flapping wing in the flapping arc; $\mathbf{V}_{\text{rf}}$ is the V_i or U_i for each direction; and $\mathbf{V}_{\text{XYZ}}$ (v_{xi} or v_{yi}) is the velocity from PIV, which is the velocity with respect to the inertial frame. From Eq. (12), $\mathbf{V}_{xyz} = \mathbf{V}_{\text{XYZ}} - \mathbf{V}_{\text{rf}}$, and $\mathbf{V}_{\text{XYZ}}$ can be calculated at each control surface. Equation (16) shows only the force in the y direction; the force in the x direction of the flapping wing is obtained using the same method.

From the conservation of mass,

$$\frac{\partial}{\partial t}\int_{\text{CV}} \rho\,\text{d}\cancel{V} + \int_{\text{CS}} \rho\mathbf{V}_{xyz}\cdot\,\text{d}\mathbf{A} = 0 \tag{17}$$

When density ρ and volume $\cancel{V}$ are constant, the conservation of mass for incompressible flow through a fixed control volume becomes

$$\int_{\text{CS}} \rho\mathbf{V}_{xyz}\cdot\,\text{d}\mathbf{A} = 0 \tag{18}$$

The conservation of mass is satisfied in three dimensions (spanwise and chordwise planes). However, if steady state is assumed, in satisfying the conservation of mass, the time rate of change of the momentum inside the control volume,

$$\frac{\partial}{\partial t}\int_{\text{cv}} \mathbf{V}_{\text{XYZ}}\rho_{\text{cv}}\,\text{d}\cancel{V}$$

is zero, and the net rate of momentum flux out through the control surface (in three dimensions),

$$\int_{\text{cs}} \mathbf{V}_{\text{XYZ}}\rho_{\text{cs}}\mathbf{V}_{xyz}\cdot\,\text{d}\mathbf{A}$$

also approaches zero. Therefore, the net lift force in three dimensions for steady flow is equal to the pressure/shear force for the control volume defined.

Results

Spanwise Lift Force Distribution

As can be clearly seen in Fig. 11, there is significant flow in the spanwise plane over the wing (wing no. 1 at a 4-Hz flapping frequency) near the middle of the downstroke. The velocity vectors were obtained at a height of 9 mm (4.5% of b) off of the wing surface. The y component of normalized velocity just off the lower and upper surfaces of the wing is essentially proportional to the tangential velocity of the wing (Fig. 11b). However, the normalized spanwise velocity (velocity parallel to the wing) over the upper surface of the wing is substantially greater than the normalized spanwise velocity just off of the lower surface of the wing (Fig. 11a) in the downstroke. Figure 11 shows the normalized velocity component distribution along the wing semispan at a $\Phi = -2$ deg in the downstroke at a 4-Hz flapping frequency ($Re = 14,700$) with wing no. 1.

Figure 12 shows the calculated spanwise lift coefficient distribution on the wing semispan determined by substituting PIV data (speed of $\sqrt{u^2 + v^2}$) into the preceding methods for pressure/shear and momentum flux along the entire semispan at a fixed point in the flapping arc. The lift coefficient distribution shows the direct contribution of flow in the spanwise plane toward the generation of lift. The sum of the net rate of momentum flux and pressure/shear force is equal to the net lift force in steady state for the case in which mass is conserved, as shown in Eq. (15). The conservation of mass is satisfied in three dimensions (combined spanwise and chordwise planes), and the net rate of momentum flux out through the control surface,

$$\int_{cs} \mathbf{V}_{XYZ} \rho_{cs} \mathbf{V}_{xyz} \cdot \mathrm{d}\mathbf{A}$$

approaches zero. Thus, the net lift force in three dimensions is equal to the pressure/shear force. However, conservation of mass in the two-dimensional plane (spanwise plane) considered is not naturally satisfied. Therefore, the force distribution using the net rate of change of momentum flux is not quite exact in the two-dimensional plane. This problem is similar to that found by Van Oudheusden et al. [15], in which difficulty was encountered conserving mass in the application of PIV to a control-volume approach to force calculation due to a uniform freestream over a purely two-dimensional wing profile. At this point, it is important to note that some chordwise flow was documented when chordwise planes were studied along the span. Through calculations associated with Hong and Altman [8], chordwise flow was shown to have no significant effect on the results.

Flat-Plate and Spanwise-Cambered Wings

Most aircraft and bird wings are cambered in chord to generate more lift at lower angles of attack. The effects of cambering wings in the chordwise sense are well-documented. However, the effects of cambering wings in the spanwise direction are not frequently discussed. Spanwise camber is observed in the flight of most birds, bats, and insects. Insects have been found to have up to 4% camber in span [18]. Dudley [19], Pennycuick [20], Combes [21], and Daniel [22] discussed the advantages of having wings curved in span. Ennos [23] showed that the presence of spanwise bending due to the inertia of flapping wings could produce at least twice as much aerodynamic force as that in rigid wings.

In this section, the experiments performed to compare the aerodynamic lift force generated by pure flapping of a spanwise-cambered wing and a flat-plate wing will be discussed. The cambered and flat-plate wings have the same mass, material, area, and aspect ratio (wing nos. 4 and 6 in Table 1). The cambered wing was only cambered in the spanwise direction, and the high-speed camera was used to verify that minimal wing deflection occurred throughout both the up- and downstrokes. Velocity was acquired in the last 1 cm ($y/b = 0.93$) of the tip of the flapping wing (where peak spanwise velocities were observed) to quantitatively compare the differences in the cambered and flat-plate wings near the tip. Because of the reflection of the laser off of the wing surface, the velocity vectors were obtained at a height of 4 mm (2.6% of wing length) off of the wing surface. Coefficients of determination calculated across all frequencies and tests ranged from 0.92 to 0.93.

A representative set of results can be seen in Fig. 13. It is first noted that the curves are polynomial curve fits of the experimentally derived data, broken up into the up- and downstrokes. Thus, some of the curves do not match up precisely between the two graphs in areas in which the experimentally derived results were continuous.

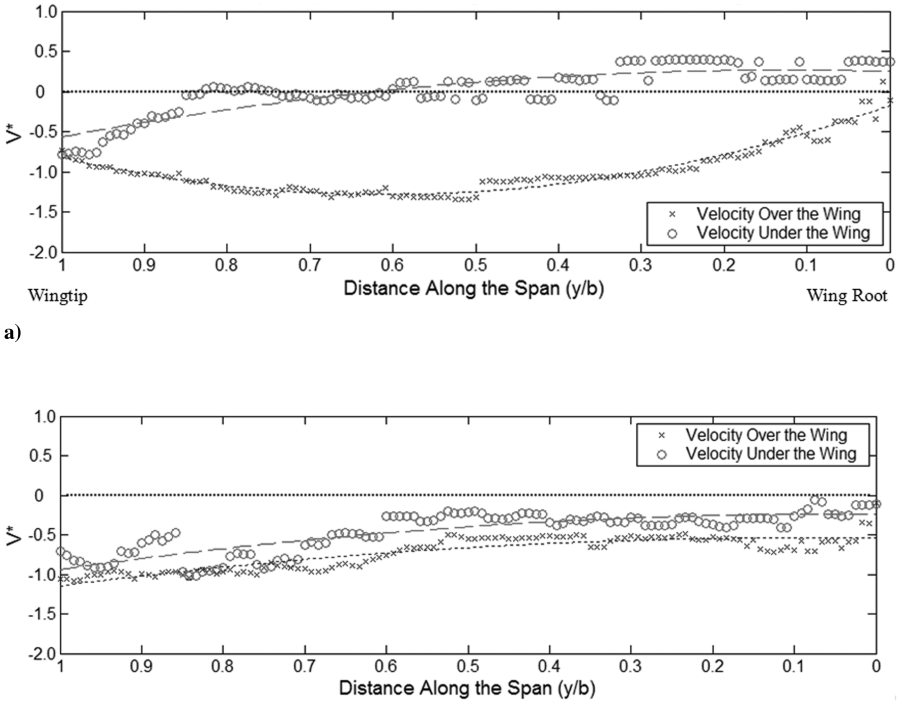

Fig. 11 Normalized velocity component distribution along the wing semispan at a $\Phi = -2$ deg in the downstroke at a 4-Hz flapping frequency ($Re = 14,700$) with wing no. 1: a) parallel to the wing (spanwise flow) and b) perpendicular to the wing.

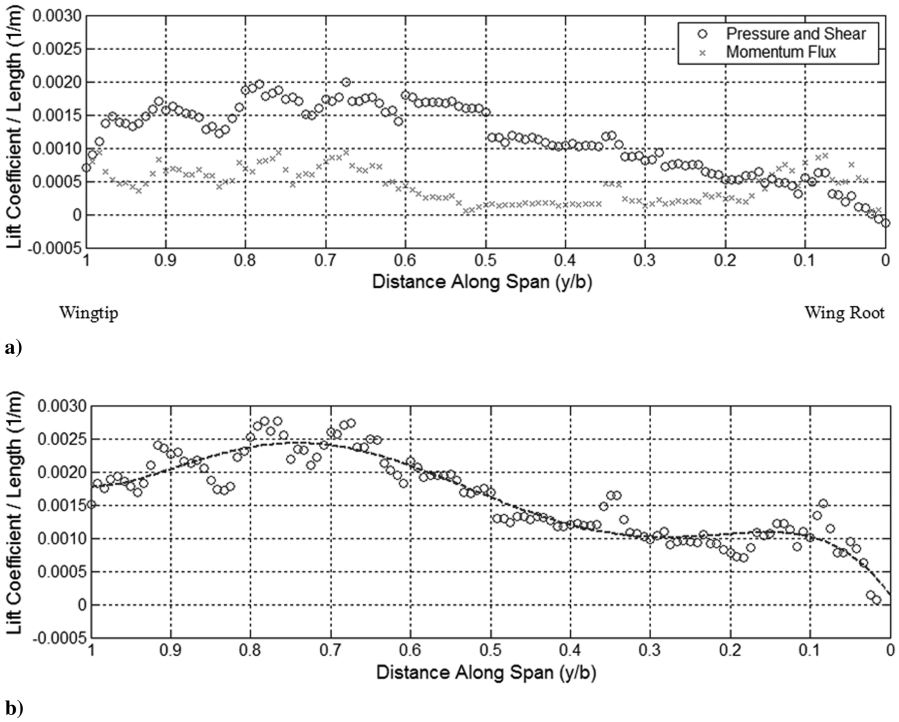

Fig. 12 Lift coefficient distribution along the wing at a $\Phi = -2$ deg in the downstroke arc at a 4-Hz flapping frequency ($Re = 14,700$) with wing no. 1: a) pressure and shear distribution method and the net rate of change of momentum flux applied to a control-volume method (two dimensions in the spanwise plane) and b) the sum of the two methods.

The temporal difference in speed (scalar value) distributions across the upper and lower surfaces between the downstroke and upstroke can readily be observed, with the downstroke experiencing a much greater difference. This is likely due to the stroke asymmetry discussed previously. In addition, when comparing the cambered- and uncambered-wing cases in the downstroke, the greater speed difference from the upper to lower surfaces exists earlier in the stroke for the cambered-wing case. Applying the simplified model (Bernoulli's equation) using speed $\sqrt{v_x^2 + v_y^2}$, it follows that for the set of points being considered, greater force is generated locally in the upward direction (lift) earlier in the downstroke in the cambered-wing case. For the unfeathered flapping wing during the upstroke, the differences are much smaller and difficult to distinguish; however, early in the upstroke, there are strong effects resulting from artifacts from the downstroke creating greater speed differences. These effects would presumably be strongly influenced by the flapping frequency and stroke asymmetry.

As can be observed in Fig. 14, the transient upper-to-lower-surface spanwise speed difference is directly related to the generation of normalized lift. It is therefore expected that the cambered wing and the flat wing will have different transient variation in aerodynamic force during the flapping cycle. Figure 14 shows the calculated temporal variation in normalized lift force through the flapping cycle resulting from the normal force N approximated using Bernoulli's equation and the axial force A approximated using the shear stress during the full flapping cycle. In Fig. 14a, the cambered wing shows a peak lift coefficient much earlier in the downstroke than with the flat-plate wing. Both the cambered and flat wings produce another peak force almost at the end of the downstroke.

Both wings generate another local peak lift force at the beginning of the upstroke, as seen in Fig. 14b. Otherwise, there is little noticeable difference in the lift coefficient due to normal force in the upstroke. From observing the axial force variation, it can be inferred that the airflow runs parallel to the wing surface at the beginning and end of each stroke. Figures 14c and 14d show the axial force of the flat wing to be slightly greater than that of the cambered wing near the beginning of the downstroke and at the end of the upstroke. The axial force of the cambered wing is, in fact, greater than that of the flat wing throughout most of the downstroke and the beginning of the

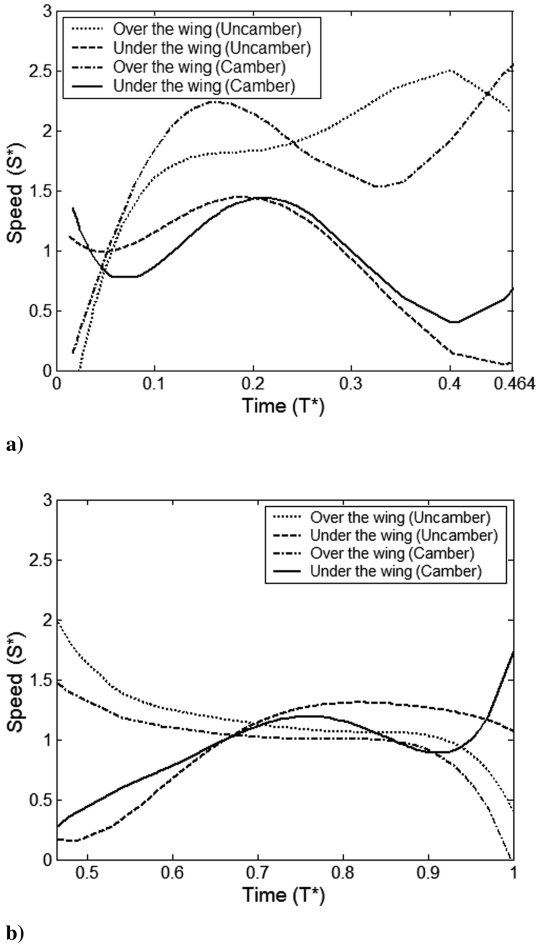

Fig. 13 Normalized spanwise speed variation over the upper and lower surfaces of the wing for the cambered and flat-plate wings in pure flapping in quiescent air for wing nos. 4 and 6 at a 4-Hz flapping frequency and $Re = 6310$: a) downstroke and b) upstroke.

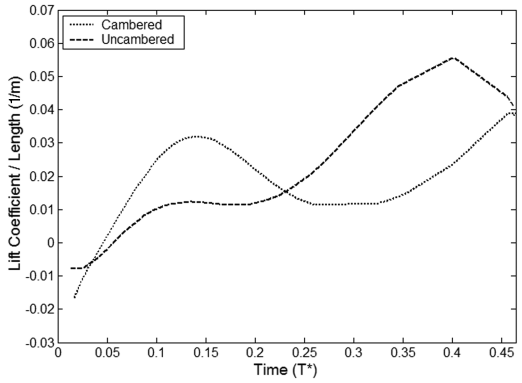

a)

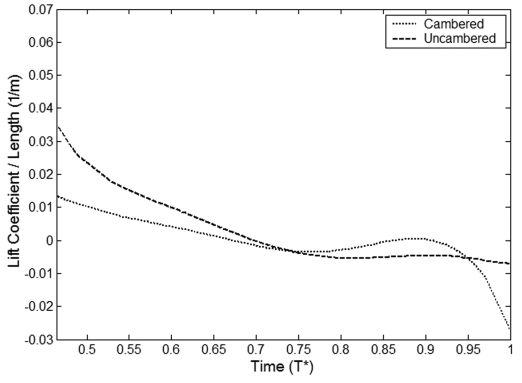

b)

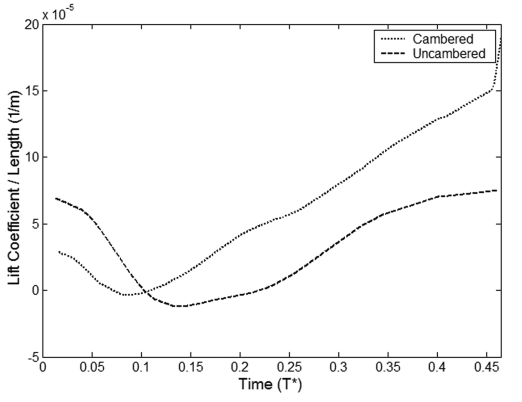

c)

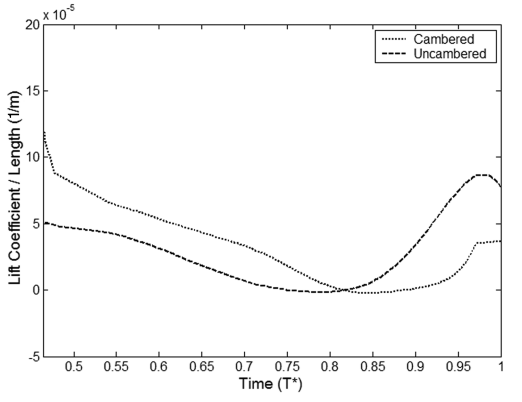

d)

Fig. 14 Lift coefficient variation due to the normal and axial forces in cambered and flat wings calculated from PIV velocity vectors for wing nos. 4 and 6 at a 4-Hz flapping frequency: a) normal force during the downstroke, b) normal force during the upstroke, c) axial force during the downstroke, and d) axial force during the upstroke.

upstroke. Near the end of the upstroke, the flat and cambered wings produce a negative lift force once again. However, the magnitude of the axial force coefficient is two orders of magnitude smaller than that of the normal force coefficient. The most important observation from Fig. 14 is the sharp difference in transient normalized force as a result of the presence of spanwise camber.

The results in Fig. 15 compare the results in Fig. 14 with the general trends in lift coefficient variation due to the aerodynamic force seen previously (in Fig. 7b), obtained using the high-speed camera and force transducer. When taken together, the results for this method confirm that camber in span can fundamentally affect the transient lift produced by a wing during the downstroke when compared with that of a flat (uncambered) wing.

Velocity data for calculating the force were acquired in the last 1 cm of the tip of the flapping wing ($y/b = 0.93$). The interrogation area for one velocity vector was 0.14×0.14 cm. The force variation due to the aerodynamic force obtained using the high-speed camera and force transducer is measured from a wing with dimensions of 15.5×10 cm. Therefore, the force calculated using normal force and momentum flux is multiplied by 120 to qualitatively scale the curves for the purposes of comparison. This scaling provides some insight into the maximum order of magnitude of the forces possible.

In the downstroke, the increase in lift coefficient due only to momentum flux increases rapidly in the first 15% of the downstroke and then decreases gradually throughout the remainder of the downstroke. The contribution of this effect remains reasonably constant throughout the upstroke and begins to increase slightly toward the end of the upstroke. Thus, the greatest differences in lift coefficient seen due to the momentum flux method were seen in the locations in the stroke with the greatest acceleration (due to stroke asymmetry). The greatest contribution of normal force occurred at

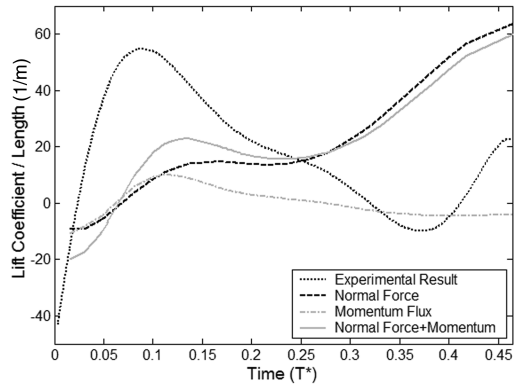

a)

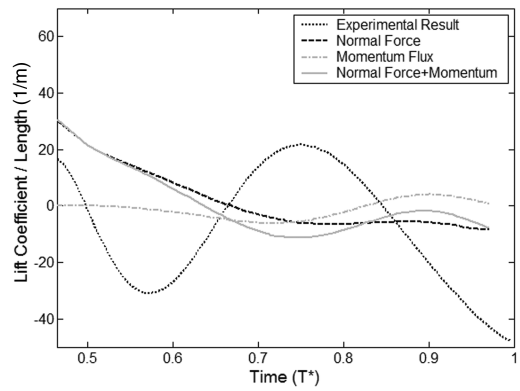

b)

Fig. 15 Comparison of lift coefficient variation due to the aerodynamic force obtained using three methods: high-speed camera and force transducer (experimental), normal force N calculated with speed $\sqrt{u^2 + v^2}$, and momentum flux for wing no. 4 at a 4-Hz flapping frequency with $Re = 6310$ during the a) downstroke and b) upstroke.

the downstroke-to-upstroke stroke reversal, although there was an increase in lift coefficient due to normal force in the first 15% of the downstroke as well.

Conclusions

A thin flat plate and thin cambered plate were simply flapped in quiescent air and without chordwise pitch change. Two different methods were presented that use PIV results to determine the aerodynamic forces due exclusively to flow in the spanwise direction from the flapping motion: 1) the direct evaluation of the pressure and the shear stress on the surface of the wing and 2) a net rate of change of momentum flux using a moving control volume. It was shown that spanwise flow is responsible for the generation of lift during the flapping motion. The effect of cambering a flapping wing in span was shown to greatly affect the phase with which peak aerodynamic force is created in the flapping arc. It follows that there is the possibility of a similar effect on the generation of lift in the spanwise plane in flapping animals. Regardless, exploitation of this effect should be further investigated for use in artificial flapping-wing MAVs.

References

[1] *Biologically Inspired Flight for Micro Air Vehicles* [CD-ROM], U.S. Air Force Office of Scientific Research, Wright–Patterson AFB, OH, June 2006.

[2] Birch, J. M., and Dickinson, M. H., "Spanwise Flow and the Attachment of the Leading-Edge Vortex on Insect Wings," *Nature (London)*, Vol. 412, No. 6848, Aug. 2001, pp. 729–733. doi:10.1038/35089071

[3] Ellington, C. P., Van Den Berg, C., Willmott, A. P., and Thomas, A. L. R., "Leading Edge Vortices in Insect Flight," *Nature (London)*, Vol. 384, No. 6610, Dec. 1996, pp. 626–630. doi:10.1038/384626a0

[4] Taylor, G. S., Schnorbus, T., and Gursul, I., "An Investigation of Vortex Flows over Low Sweep Delta Wings," AIAA Paper 2003-4021.

[5] Birch, J. M., Dickson, W. B., and Dickinson, M. H., "Influence of Re on the Forces and Flows Around Flapping Wings," *The Journal of Experimental Biology*, Vol. 207, 2004, pp. 1063–1072. doi:10.1242/jeb.00848

[6] Greenewalt, C. H., *Dimensional Relationships for Flying Animals*, Smithsonian Inst., Washington, D.C., 1962.

[7] Azuma, A., *The Biokinetics of Flying and Swimming*, Springer–Verlag, New York, 1992.

[8] Hong, Y., and Altman, A., "Streamwise Vorticity in Simple Mechanical Flapping Wings," *Journal of Aircraft*, Vol. 44, No. 5, Sept.–Oct. 2007, pp. 1588–1597.

[9] Sane, S. P., and Dickinson, M. H., "The Control of Flight Force by a Flapping Wing: Lift and Drag Production," *The Journal Of Experimental Biology*, Vol. 204, No. 15, 2001, pp. 2607–2626.

[10] Westerweel, J., *Digital Particle Image Velocimetry—Theory and Application*, Delft Univ. Press, Delft, The Netherlands, 1993.

[11] Alford, L., and Altman, A., "A New Investigation of Natural Flight Characteristics and Theory," SAE Aerospace Division Conference, Reno, NV, Society of Automotive Engineers Paper 2004-01-3089, Sept. 2004.

[12] Maybury, W. J., and Lehmann, F.-O., "The Fluid Dynamics of Flight Control by Kinematic Phase Lag Variation Between Two Robotic Insect Wings," *The Journal of Experimental Biology*, Vol. 207, No. 26, 2004, pp. 4707–4726. doi:10.1242/jeb.01319

[13] Noca, F., Shiels, D., and Jeon, D., "Measuring Instantaneous Fluid Dynamic Forces on Bodies, Using Only Velocity Fields and Their Derivatives," *Journal of Fluids and Structures*, Vol. 11, No. 3, 1997, pp. 345–350. doi:10.1006/jfls.1997.0081

[14] Unal, M. F., Lin, J. C., and Rockwell, D., "Force Prediction by PIV Imaging: A Momentum-Based Approach," *Journal of Fluids and Structures*, Vol. 11, No. 8, 1997, pp. 965–971. doi:10.1006/jfls.1997.0111

[15] Van Oudheusden, B. W., Scarano, F., Casimiri, E. W. F., "Non-Intrusive Load Characterization of an Airfoil Using PIV," *Experiments in Fluids*, Vol. 40, No. 6, 2006, pp. 988–992. doi:10.1007/s00348-006-0149-2

[16] Gurka, R., Liberzon, A., Hefetz, D., Rubinstein, D., and Shavit, U., "Computation of Pressure Distribution Using PIV Velocity Data," *Proceedings of the Third International Workshop on Particle Image Velocimetry (PIV'99)*, 1999, pp. 671–676.

[17] Ellington, C. P., "The Novel Aerodynamics of Insect Flight: Applications to Micro-Air Vehicles," *Journal of Experimental Biology*, Vol. 202, No. 23, 1999, pp. 3439–3448.

[18] Combes, S. A., and Daniel, T. L., "Flexural Stiffness in Insect Wings 2: Spatial Distribution and Dynamic Wing Bending," *The Journal of Experimental Biology*, Vol. 206, No. 17, 2003, pp. 2989–2997. doi:10.1242/jeb.00524

[19] Dudley, R., *The Biomechanics of Insect Flight: Form, Function, Evolution*, Princeton Univ. Press, Princeton, NJ, 2000.

[20] Pennycuick, C. J., "Animal Flight," *The Institute of Biology's Studies in Biology*, Vol. 33, Edward Arnold, London, 1972.

[21] Combes, S. A., "Wing Flexibility and Design For Animal Flight," Ph.D. Thesis, Univ. of Washington, Seattle, WA, 2002.

[22] Daniel, T. L., "Forward Flapping Flight from Flexible Fins," *Canadian Journal of Zoology*, Vol. 66, No. 3, 1988, pp. 630–638.

[23] Ennos, A. R., "Inertial and Aerodynamic Torques on the Wings of Diptera in Flight," *The Journal of Experimental Biology*, Vol. 142, No. 1, 1989, pp. 87–95.